

Constraining gas motions in the Centaurus cluster using X-ray surface brightness fluctuations and metal diffusion

S. A. Walker,^{1*} J. S. Sanders² and A. C. Fabian¹

¹*Institute of Astronomy, Madingley Road, Cambridge CB3 0HA*

²*Max-Planck-Institute für extraterrestrische Physik, 85748 Garching, Germany*

ABSTRACT

We compare two different methods of constraining the characteristic velocity and spatial scales of gas motions in the X-ray bright, nearby Centaurus cluster, using new deep (760ks) Chandra observations. The power spectrum of excess surface brightness fluctuations in the 0.5–6.0 keV band in a sector to the west is measured and compared to theoretical expectations for Kolmogorov index fluctuations. The observed power spectrum is flatter than these expectations, and the surface brightness fluctuations are around the 8 percent level on length scales of 2 kpc. We convert the 2D power spectrum of fluctuations into a 3D power spectrum using the method of Churazov et al., and then convert this into constraints on the one-component velocity of the gas motions as a function of their length scale. We find one-component velocities in the range 100–150 km/s on spatial scales of 4–10 kpc. An independent constraint on the characteristic velocity and length scales of the gas motions is then found by considering the diffusion coefficient needed to explain the distribution of metals in the Centaurus cluster, combined with the need to balance the rate of gas cooling with the rate of heat dissipated by the gas motions. We find that these two methods of constraining the velocity and length scales of the gas motions are in good agreement.

Key words: galaxies: clusters: individual: Centaurus - galaxies: clusters: intracluster medium - intergalactic medium - X-rays: galaxies: clusters.

1 INTRODUCTION

In the centres of galaxy clusters the cooling time of gas is much shorter than the Hubble time. Feedback from the central AGN is needed to counteract this cooling to prevent the formation of a cooling flow and limit the rate of star formation. The precise way in which the AGN feedback energy is dissipated into the intracluster medium (ICM), and how this can so accurately balance the rate of cooling, remains under debate.

Turbulence is one mechanism through which the energy from the central AGN could be dissipated into the ICM to counteract cooling. Direct constraints on the level of turbulence in the cores of galaxy clusters remain challenging with existing X-ray instruments. Measuring the width of emission lines seen with the RGS (reflection grating spectrometer) instrument on *XMM-Newton* can provide upper limits on the level of gas motions. Sanders et al. (2010) used this method to find a limit of 274 km s⁻¹ for random gas motions in the core of Abell 1835, while in the sample of

clusters studied in Sanders et al. (2011) 15 clusters were found for which the upper limits gave a turbulence to thermal energy density ratio of less than 20 percent.

Recent high spatial resolution studies of nearby clusters have investigated spatial fluctuations in the X-ray emission from the centres of galaxy clusters, which can place limits on the level of gas motions in the ICM due to turbulence. Churazov et al. (2012) studied the X-ray surface brightness fluctuations in the core of the non-cool core Coma cluster with *Chandra* and *XMM-Newton* data, using the Δ -variance technique (Stutzki et al. 1998) to characterise the magnitude of fluctuations as a function of their spatial scale. They found that the characteristic amplitude of excess density fluctuations varied from ~ 5 percent on scales of ~ 30 kpc, up to 7–10 percent on much larger scales of ~ 500 kpc.

Sanders & Fabian (2012) investigated the X-ray surface brightness fluctuations in the cool-core galaxy cluster AWM7, and found implied 3D density density fluctuations with a standard deviation of around 4 percent, with 3D pressure variations of at most 4 per cent as well. They compared the shape of the power spectrum of excess surface brightness fluctuations with that expected from

* Email: swalker@ast.cam.ac.uk

Kolmogorov index fluctuations, and found the observed spectrum to be flatter than these expectations. By comparing the northern and southern sectors of AWM7, they found significant spatial variations in the fluctuations. In the northern sector studied, there was a factor of 2 less Δ -variance relative to the southern sector studied.

Recently, Zhuravleva et al. (2014) and Zhuravleva et al. (2015) have studied the X-ray surface brightness fluctuations in the Perseus and Virgo clusters. In Zhuravleva et al. (2014) the 2D power spectrum of surface brightness fluctuations is converted into a 3D power spectrum, which is subsequently converted into the one-component velocities of the gas motions needed to cause the fluctuations, which are found as a function of their spatial size. This method was applied to annuli of increasing radius, and the characteristic one-component velocity was found to decrease from around 200 km/s in the central 30 kpc to 100 km/s at a distance of 200 kpc from the centre. They then calculated the turbulent heating rate expected for gas motions with the velocity and spatial sizes found. For the Perseus and Virgo clusters, they find that the rate of turbulent heating deduced using this method is roughly equal to the cooling rate of the gas in all of the radial annuli studied, adding support to the idea that turbulence plays a role in balancing gas cooling in cluster cores.

Independent constraints on the velocity and spatial scales of the gas motions can also be found from the distribution of metals in the abundance peak around the brightest cluster galaxy, BCG (Rebusco et al. 2005, Rebusco et al. 2006). This method assumes that, as the metals are continuously deposited into the ICM from stars in the BCG over the life time of the cluster, the profile of the metal abundance from this deposition follows the light profile of the BCG. The metals then diffuse outwards to form the much broader metal abundance peaks in cluster cores that we see today. By assuming that metal diffusion has proceeded through stochastic gas motions, this allows the metal diffusion coefficient, D to be constrained, which is proportional to the product of the characteristic velocity, v , and length scales, l , of these gas motions. If it is then assumed that the heating rate from the dissipation of these stochastic gas motions balances the gas cooling rate, v and l can be constrained. Rebusco et al. 2005 used this technique for the Perseus cluster and found that a diffusion coefficient of $2 \times 10^{29} \text{ cm}^2 \text{ s}^{-1}$ is needed to explain the observed abundance profile. They deduced that the turbulent gas motions in Perseus have velocities of $\sim 300 \text{ km s}^{-1}$ on spatial scales of 20 kpc.

Here we investigate new, deep (760 ks) Chandra observations of the cool-core Centaurus cluster (P.I J.S. Sanders) to compare the constraints on the characteristic velocity and spatial scales of gas motions obtained by considering the X-ray surface brightness fluctuations and the distribution of metals in the ICM. A detailed study of these new Chandra observations will be presented in Sanders et al. (submitted). Centaurus' proximity (it is the second nearest galaxy cluster), combined with its high X-ray flux makes it an ideal target for exploring X-ray surface brightness fluctuations.

Graham et al. (2006) have previously used the existing 200ks Chandra observation to investigate metal diffusion following the method of Rebusco et al. (2005). The azimuthally averaged metal abundance profile for Centaurus has a prominent drop between 20-50 kpc from the core which requires a comparatively low diffusion coefficient to maintain. Graham et al. (2006) found a best fitting diffusion coefficient in the range $2-4 \times 10^{28} \text{ cm}^2 \text{ s}^{-1}$, nearly an order of magnitude lower than that found for Perseus in Rebusco et al. (2005). The very high metallicity around the BCG of Centaurus, which peaks at nearly $3 Z_{\odot}$ (Fabian et al. 2005), makes it an excellent target for applying this method.

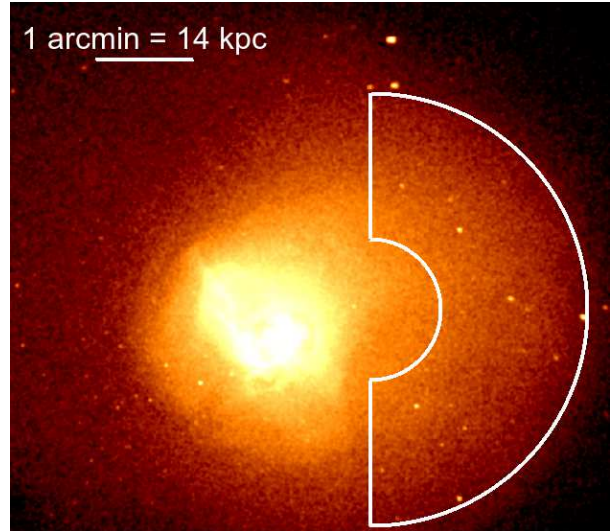


Figure 1. Exposure corrected 0.5-6.0 keV mosaic image of the Centaurus cluster. The white sector region shown is used for the analysis of the surface brightness fluctuations. Point sources have not been removed from this image.

Table 1. Chandra observations used

Obsid	Cleaned exposure/ ks	Date
504	26	2000-05-22
505	10	2000-06-08
4190	34.1	2003-04-18
4191	33.8	2003-04-18
4954	85.4	2004-04-01
4955	43.1	2004-04-02
5310	48.7	2004-04-04
16223	176.2	2014-05-26
16224	41.2	2014-04-09
16225	29.7	2014-04-26
16534	55	2014-06-05
16607	44.6	2014-04-12
16608	33.3	2014-04-07
16609	81.7	2014-05-04
16610	17.1	2014-04-27
Total	760	

We use a standard Λ CDM cosmology with $H_0 = 70 \text{ km s}^{-1} \text{ Mpc}^{-1}$, $\Omega_M = 0.3$, $\Omega_{\Lambda} = 0.7$. For the redshift of the Centaurus cluster, $z = 0.011$, the luminosity distance is 49.5 Mpc and the angular scale is 0.235 kpc/arcsec. All errors unless otherwise stated are at the 1σ level.

2 DATA

The new deep Chandra observations of Centaurus will be presented and explored in depth in Sanders et al. (submitted). The observations used are tabulated in table 1. The data were reprocessed using CIAO v4.6. Lightcurves for each observation were examined, with any periods deviating from the standard deviation by more than 2.5σ removed, leaving a total clean exposure of 760ks.

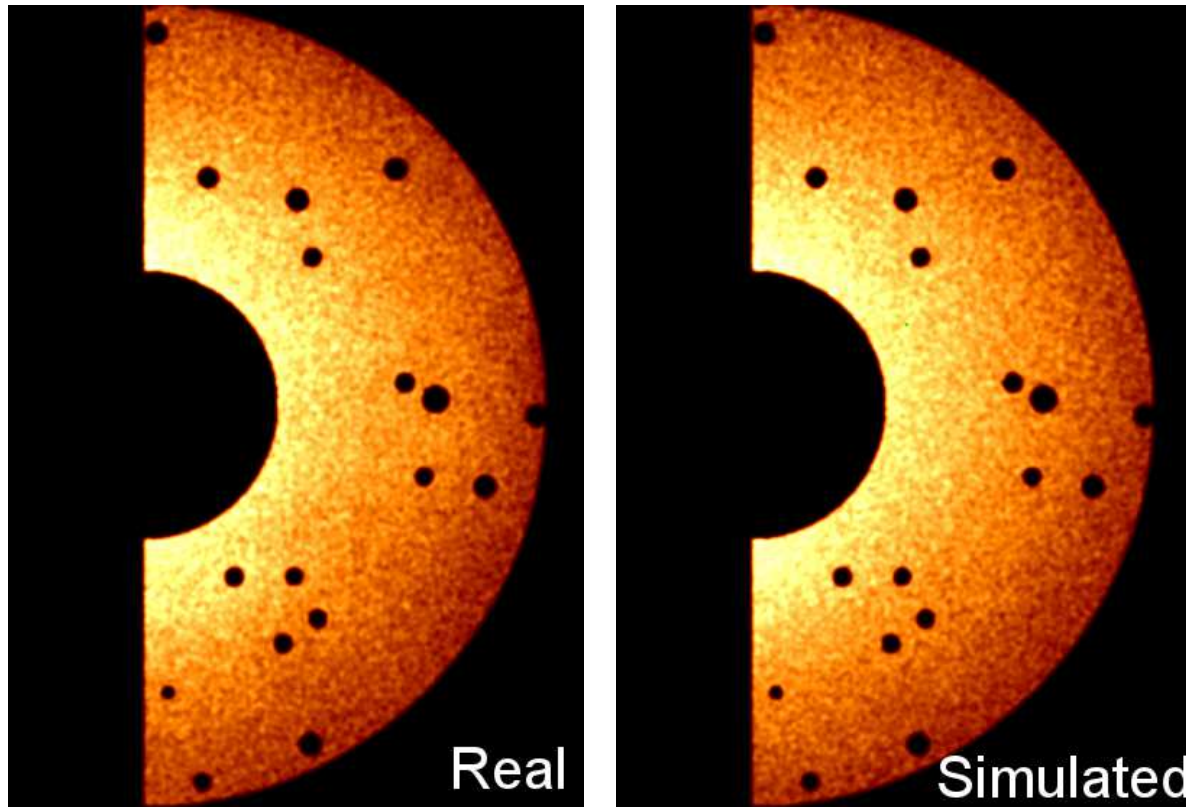


Figure 2. Left: Actual 0.5-6.0keV band image from the sector region shown in Fig. 1, with point sources removed. Right: Simulated 0.5-6.0keV band image from the same sector, obtained by modelling the surface brightness of this region with 10 ellipsoids.

3 ANALYSIS

The exposure corrected and background subtracted 0.5-6.0 keV band stacked image of Centaurus is shown in Fig. 1. The stacked, exposure corrected image was produced following the methods described in Walker et al. (2014). To study the surface brightness fluctuations we investigate the region shown by the white sector, which spans a radial range of 23-43 kpc from the centre of the BCG. This region lies between the core and the large western cold front. It has a high X-ray surface brightness over a large area and is relatively smooth in its X-ray emission. It was chosen to avoid any surface brightness features which are obviously due to feedback from the core (i.e. the cavities and filaments) or due to gas sloshing (i.e. the eastern and western cold fronts and the ‘bay’ feature to the south west of the core).

The left hand panel of Fig. 2 shows the sector region by itself, with point sources removed. Point sources were identified by the tool `wavdetect`, using a range of wavelet sizes between 1 and 16 pixels. The large scale surface brightness distribution in this region was modelled by fitting ten ellipsoids to it, producing a smooth model image. This ten ellipsoid model was used because it was found to be the simplest way of accurately modelling the large scale surface brightness distribution of the region. The power spectrum of this model on large scales matches that of the real observations very closely. This smooth model image was multiplied by the exposure map, and then a simulated image in the 0.5-6.0 keV band was obtained by making a Poisson realisation. This was then exposure corrected by dividing by the exposure map, producing the simulated image shown in the right hand panel of Fig. 2.

In Fig. 3 we show the ratio of the real image (left) and the simulated image (right) to the smooth image we obtained by fitting 10 ellipsoids to this region. There are clear structures in the residuals of the real data to this smooth model (left hand panel) at the 10 percent level.

4 COMPARING FLUCTUATION POWER SPECTRA

To compare the shape and magnitude of the observed power spectrum of surface brightness fluctuations with theoretical expectations for hydrodynamical turbulence, we follow the approach of Sanders & Fabian (2012). We use the simulated image of the sector, obtained by fitting 10 ellipsoids to the region, and add to it surface brightness fluctuations with a powerlaw power-spectrum. These surface brightness fluctuations are generated by finding the fast Fourier transform of a cube of dimensions $700 \times 700 \times 700$, which is larger than the size of the region of the Centaurus image explored (in terms of pixels). Each pixel in the cube was scaled by a powerlaw power spectrum of index $-11/3$ (the shape expected for the electron density power spectrum for a Kolmogorov process), using a normal distribution for the real and imaginary components. Following the inverse transform, the real component for each pixel was taken. The powerspectrum was truncated to remove structure on scales larger than 30 kpc (the radial range spanned by the sector examined). We ensured that this truncation scale is consistent with the use of the 10 ellipsoids model for removing large-scale perturbations.

We deproject the surface brightness profile from the Cen-

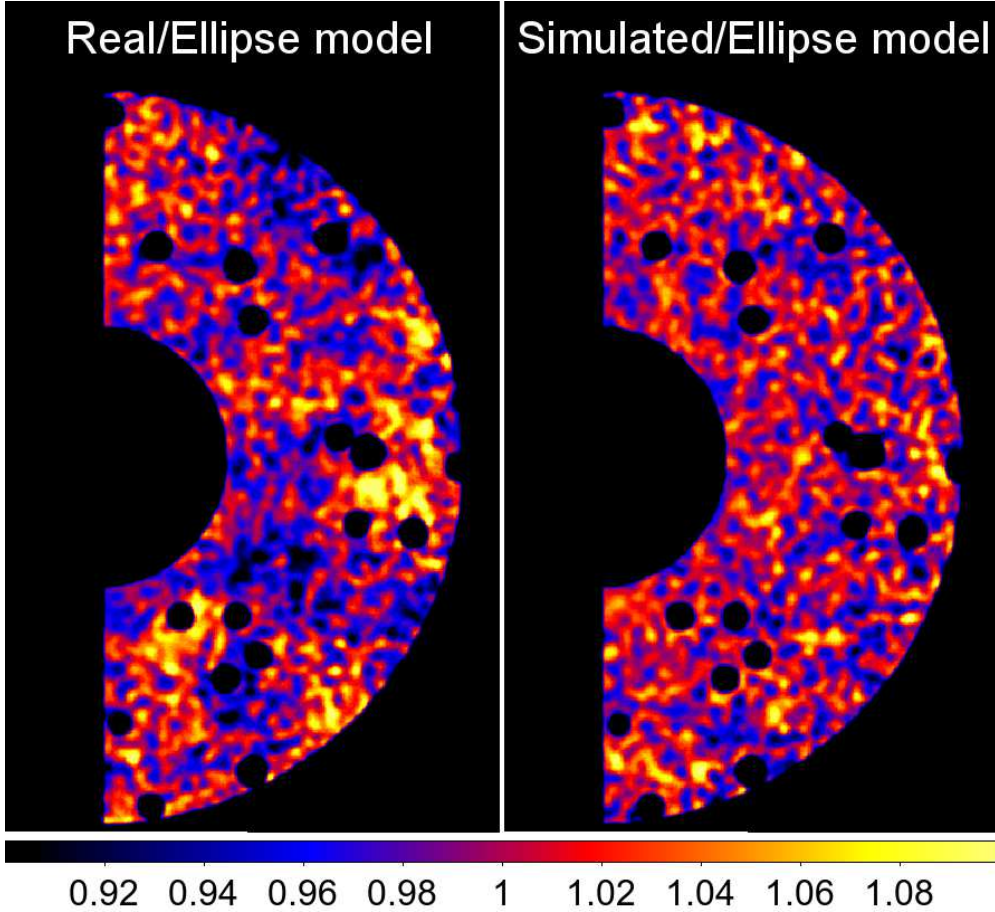


Figure 3. Left: Ratio of the actual data to the best fitting 10 ellipsoidal model. Right: Ratio of the simulated data to the best fitting 10 ellipsoidal model.

taurus observations to obtain the deprojected emissivity model, $E(x, y, z)$. We then integrate the cubic fluctuation, $F(x, y, z)$ (normalised to have a standard deviation of 1), field along the z -axis, multiplying by the deprojected emissivity profile and a scale factor determining the magnitude of input fluctuations, ϵ ,

$$S(x, y) = \int [1 + \epsilon F(x, y, z)] E(x, y, z) dz \quad (1)$$

from which we obtain a simulated image, $S(x, y)$ containing powerlaw fluctuations of magnitude 4, 8 and 16 percent in surface brightness. The Chandra exposure maps were then used to create Poisson realisations of these images, allowing us to compare these to the actual observations.

We then used the delta variance technique to find the power spectra of the simulated images to which fluctuations of magnitude 4, 8 and 16 percent in surface brightness have been added. These magnitudes correspond to the RMS of the surface brightness over the image. These power spectra are shown in Fig. 4. The power spectrum of the simulated ellipsoidal model with zero fluctuations has been subtracted from these power spectra, allowing us to see the excess power that is just due to the fluctuations we have added. The error ranges of the power spectra were calculated by simulating 1000 Poisson realisations of each image and finding the standard deviation of the power spectra from these. We performed tests to ensure the results are not sensitive to variations in the procedure

used. The analysis was repeated but this time the model was subtracted from the data first, and then the power spectrum was found. The results were found to be the same as those obtained by subtracting the power spectrum of the model from that of the data.

The power spectrum of the actual data (shown as the cyan region in Fig. 4) is then compared to these simulations of different fluctuation levels. We see that the power spectrum of the real data is flatter in shape than the spectra made assuming fluctuations using a standard Kolmogorov powerlaw index of $-11/3$. This is similar to what was found by Sanders & Fabian (2012) for AWM7. It may be possible that unresolved compact sources contribute to the apparent flatness of the observed spectrum. The 10 ellipsoidal model used only has a noticeable affect on scales larger than around 10 kpc, so it is unlikely that the use of this model contributes to the observed flattened shape.

5 VELOCITY POWER SPECTRA

Following the method detailed in Churazov et al. (2012), we can convert the 2D power spectrum obtained from our image analysis, P_{2D} , into a 3D power spectrum P_{3D} using

$$P_{2D}(k) \approx 4P_{3D}(k) \int |W(k_z)|^2 dk_z, \quad (2)$$

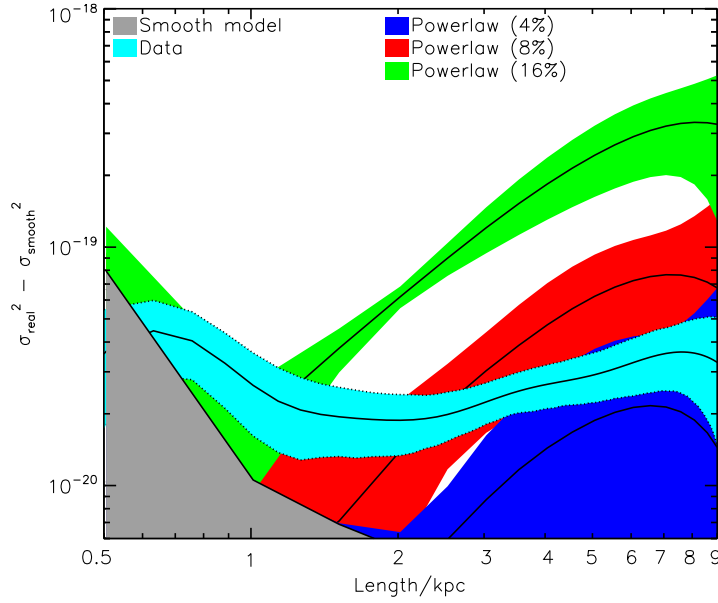


Figure 4. The power spectrum for the excess surface brightness fluctuations in the real data, from which the spectrum of the smooth model has been subtracted, is shown as the cyan region. This is compared to the power spectra of simulated images to which 4, 8 and 16 percent Kolmogorov index fluctuations have been added.

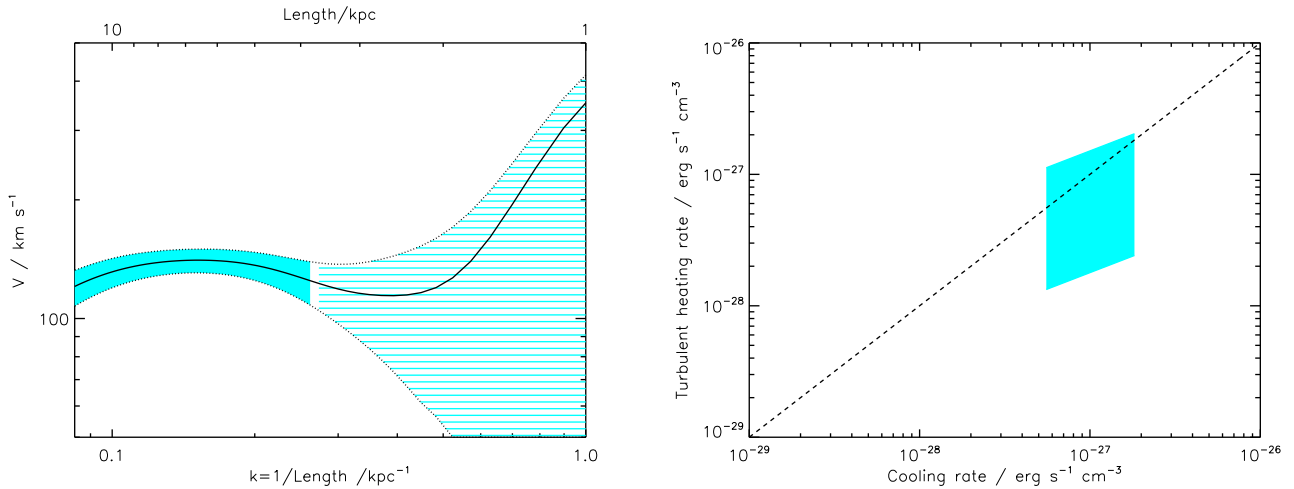


Figure 5. *Left:* Constraints on the one component velocity of the gas motions as a function of their wavenumber, derived from the power spectrum of excess surface brightness fluctuations. The solid cyan region shows the region where systematic and statistic uncertainties least affect the measurement. *Right:* The cyan region shows the turbulent heating rate inferred from the surface brightness fluctuations against the cooling rate of the sector region studied. This agrees reasonably well with equilibrium between heating and cooling, which is shown by the dashed black line.

where $|W(k_z)|^2$ is the 1D power spectrum of the normalised emissivity, $\eta(z)$, along the line of sight

$$W(k_z) = \int \eta(z) e^{-i2\pi z k_z} dz. \quad (3)$$

where $\eta(z)$ is related to the density distribution $n_0^2(x, y, z)$ by

$$\eta(x, y, z) = \frac{n_0^2(x, y, z)}{\int n_0^2(x, y, z') dz'} = \frac{n_0^2(x, y, z)}{I_0(x, y)}. \quad (4)$$

and for the small area of the cluster we consider the dependence on x and y can be neglected, such that $\eta(x, y, z) \approx \eta(z)$.

We can then follow the approach of Zhuravleva et al. (2014) and Zhuravleva et al. (2015) to convert this 3D power spectrum into the one-component velocity, $V_{1,k}$ power spectrum. For the strati-

fied atmospheres of relaxed galaxy clusters, and within the inertial range of scales, the one-component velocity is expected to be proportional to the amplitude of density fluctuations, $A_{3D} = \frac{\delta\rho_k}{\rho_0}$ at each length scale $l = 1/k$, so that we can write

$$A_{3D} = \frac{\delta\rho_k}{\rho_0} = \eta_1 \frac{V_{1,k}}{c_s} \quad (5)$$

where c_s is the sound speed. Zhuravleva et al. (2014) found using cosmological simulations of galaxy clusters that the average value of the proportionality constant η_1 is consistent with unity ($\eta_1 = 1 \pm 0.3$).

The amplitude of the density fluctuations is related to the 3D power spectrum by

$$A_{3D} = \sqrt{P_{3D}(k)4\pi k^3} \quad (6)$$

which allows us to find the amplitude of the one-component velocity of the gas motions as a function of wavenumber ($k = 1/l$) from

$$V_{1,k} \approx c_s \sqrt{P_{3D}(k)4\pi k^3} / \eta_1 \quad (7)$$

The resulting plot of $V_{1,k}$ against wavenumber is shown in the left hand panel of Fig. 5, where the solid cyan region shows where the constraint is least affected by systematic and statistic uncertainties.

In the right hand panel of Fig. 5 we show the turbulent heating rate for the sector derived from the surface brightness fluctuations using equation 10 plotted against the cooling rate for the same region. The two appear to agree reasonably well. This is similar to the findings for the Perseus and Virgo clusters studied in Zhuravleva et al. (2014).

6 CONSTRAINTS ON VELOCITY AND SPATIAL SCALES CONSIDERING METAL DIFFUSION THERMAL EQUILIBRIUM

Independent constraints on the velocities and spatial scales of the gas motions can be obtained by considering the metal diffusion coefficient, D , and the level of gas motions needed to offset cooling in the ICM. Following Rebusco et al. (2005) (who considered the Perseus cluster), under the assumption that metal diffusion is caused by stochastic gas motions on a length scale smaller than that distance from the centre of the cluster, r , we can write the diffusion coefficient in terms of the length scale, l and velocity scale, v of the gas motions

$$D \sim 0.11vl \quad (8)$$

Graham et al. (2006) applied the stochastic model of metal transport developed by Rebusco et al. (2005) to the Centaurus cluster to obtain constraints on D . This method constrains D by using the central abundance peak in galaxy clusters. The central abundance peak is likely produced by the stars in the BCG following the formation of the cluster, so the initial distribution of metals (when deposited) would be expected to follow the distribution of stars in the BCG. The observed metal peak is much broader than the light profile of the BCG, and if we assume the metals have been transported outwards by a stochastic process, constraints on D can be made by comparing the two profiles.

Graham et al. (2006) found that the best fitting diffusion coefficient had a radial dependence, decreasing with increasing radius. They found that D could be described by

$$D \approx 4 \times 10^{28} \left[\frac{n_H(r)}{n_H(r_0)} \right]^2 \text{ cm}^2 \text{ s}^{-1} \quad (9)$$

where n_H is the hydrogen density profile, and $r_0 = 25\text{kpc}$. Over the radial range of the sector we consider (23-43 kpc), D decreases from 4.7 to $1.5 \times 10^{28} \text{ cm}^2 \text{ s}^{-1}$. We can then plot the constraints on this relation between v and l , and this is shown with the black lines in the left hand panel of Fig. 6.

Another relation between v and l can be obtained by requiring the heat dissipation rate of the gas motions to balance the cooling rate. From Rebusco et al. (2005), the heating rate can be written as

$$\Gamma_{diss} \sim 0.4\rho v^3/l \quad (10)$$

from which we obtain

$$n(r)^2 \Lambda(T(r), A(r)) \sim 0.4\rho v^3/l \quad (11)$$

The red lines in the left hand panel of Fig. 6 show the constraints on v and l from this relation, where the range takes into account the range of gas density, temperature and metal abundance over the radial range of the sector considered. The constraints from equations 8 and 11 overlap in a region where they are both consistent, with heating balancing cooling and the metal diffusion coefficient agreeing with observations.

In the right hand panel of Fig. 6, we compare these constraints on v and l with those obtained earlier in Fig. 5 by considering the power spectrum of excess surface brightness fluctuations. The two different methods appear to be in good agreement with one another.

7 CONCLUSIONS

We have examined the Δ -variance power spectrum of the excess X-ray surface brightness fluctuations in a large sector to the west of the core of the Centaurus cluster, spanning a radial range between 23-43 kpc from the center of the cluster. When compared to the expected shape of the spectrum from Kolmogorov index fluctuations, the observed spectrum appears flatter. This is similar to what was found in Sanders & Fabian (2012) for the fluctuation power spectrum of AWM7. The magnitude of the surface brightness fluctuations is roughly 8 percent on scales of 2 kpc.

We have converted the 2D power spectrum into a 3D power spectrum and then found constraints on the characteristic velocity of the gas motions as a function of their spatial scaling following the methods of Churazov et al. (2012) and Zhuravleva et al. (2014). On scales between 4-10 kpc where the method is least sensitive to systematic and statistical errors, the one-component velocity of the gas motions is calculated to be in the range 100-150 km/s using this method. The turbulent heating rate from such gas motions is consistent with what is needed to balance the cooling rate, as was found for the Perseus and Virgo clusters in Zhuravleva et al. (2014).

Independent constraints on the characteristic velocity and size scale of the gas motions have been obtained by measuring the diffusion coefficient needed to explain the present day distribution of metals, and invoking equilibrium between the turbulent dissipation rate and the gas cooling rate. This involves assuming that when the metals were first deposited by the stars in the BCG their abundance profile followed the light profile of the BCG. The constraints on v

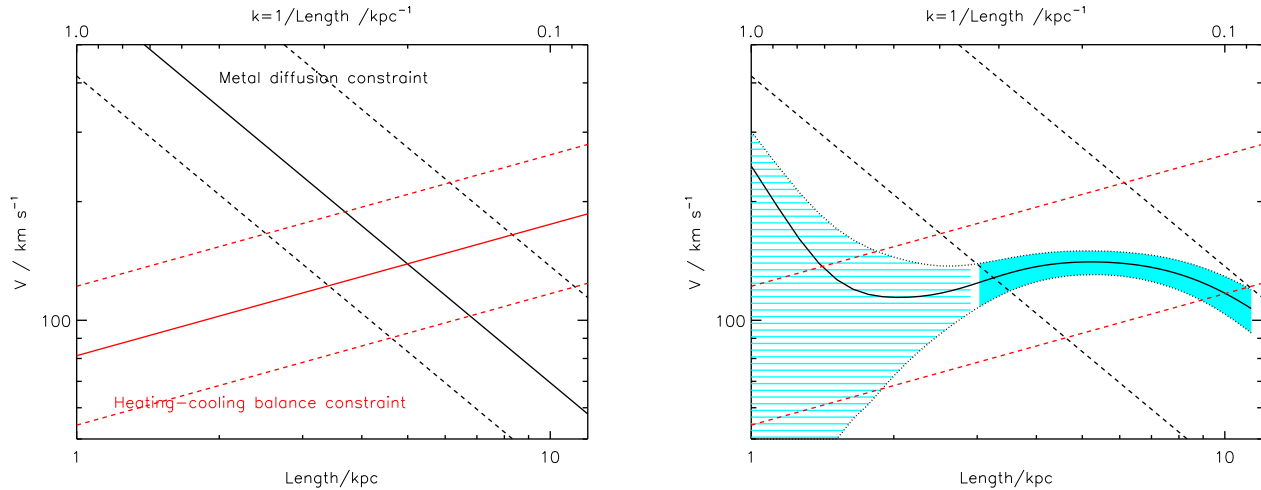


Figure 6. *Left:* The solid black line shows the relation between v and l obtained by fixing the metal diffusion coefficient in equation 8 to the best fitting value found in Graham et al. (2006) for a radius at the midpoint of the sector. The dashed black lines show the allowed range for this relation when we take into account the radial variation of the D in the sector studied, and an uncertainty of a factor of 2 in the constant coefficient in equation 8. The solid red line shows the relation obtained by equating the turbulent heating rate with the cooling rate in equation 11. The dashed red lines show the range of this relation when the radial dependence of the gas density and cooling function are factored in, along with an uncertainty of a factor of 3 in the constant coefficient in equation 11. The region where these two methods overlap provides a constraint on v and l for the gas motions *Right:* Here we overplot the constraints on v and l from the left panel onto those obtained in Fig. 5 by considering the power spectrum of excess surface brightness fluctuations.

and l obtained using this method are in reasonable agreement with those obtained from the X-ray surface brightness fluctuations.

It is possible that some fraction of the observed surface brightness fluctuations arise from sound waves rather than turbulence (Sanders et al. submitted). We investigate this in Appendix A, in which we compare the power spectrum from the whole sector with the power spectrum obtained by removing any features resembling sound waves.

ACKNOWLEDGEMENTS

SAW and ACF acknowledge support from ERC Advanced Grant FEEDBACK. This work is based on observations obtained with the *Chandra* observatory, a NASA mission.

REFERENCES

- Churazov E., Vikhlinin A., Zhuravleva I., Schekochihin A., Parrish I., Sunyaev R., Forman W., Böhringer H., Randall S., 2012, *MNRAS*, 421, 1123
- Fabian A. C., Sanders J. S., Taylor G. B., Allen S. W., 2005, *MNRAS*, 360, L20
- Graham J., Fabian A. C., Sanders J. S., Morris R. G., 2006, *MNRAS*, 368, 1369
- Rebusco P., Churazov E., Böhringer H., Forman W., 2005, *MNRAS*, 359, 1041
- Rebusco P., Churazov E., Böhringer H., Forman W., 2006, *MNRAS*, 372, 1840
- Sanders J. S., Fabian A. C., 2012, *MNRAS*, 421, 726
- Sanders J. S., Fabian A. C., Smith R. K., 2011, *MNRAS*, 410, 1797

- Sanders J. S., Fabian A. C., Smith R. K., Peterson J. R., 2010, *MNRAS*, 402, L11
- Stutzki J., Bensch F., Heithausen A., Ossenkopf V., Zielinsky M., 1998, *A&A*, 336, 697
- Walker S. A., Fabian A. C., Kosec P., 2014, *MNRAS*, 445, 3444
- Zhuravleva I., Churazov E., Arevalo P., Schekochihin A. A., Allen S. W., Fabian A. C., Forman W. R., Sanders J. S., Simionescu A., Sunyaev R., Vikhlinin A., Werner N., 2015, *ArXiv e-prints*
- Zhuravleva I., Churazov E., Schekochihin A. A., Allen S. W., Arévalo P., Fabian A. C., Forman W. R., Sanders J. S., Simionescu A., Sunyaev R., Vikhlinin A., Werner N., 2014, *Nat*, 515, 85
- Zhuravleva I., Churazov E. M., Schekochihin A. A., Lau E. T., Nagai D., Gaspari M., Allen S. W., Nelson K., Parrish I. J., 2014, *ApJ*, 788, L13

APPENDIX A: LINEAR FEATURES

Sanders et al. (submitted) have explored applying a Gaussian gradient magnitude (GGM) filter (similar to a Sobel filter) to the *Chandra* X-ray images, which emphasises gradients in the surface brightness. Sanders et al. (submitted) have identified several linear features in the northern part of the sector we have explored, which may be sound waves. This method is detailed in depth in Sanders et al. (submitted). To investigate the affect of these, we repeated our analysis by excluding these features by examining just the southern half of the sector. The results are shown in Fig. A1. In the left hand panel we compare the power spectrum of the whole sector (cyan region) with that of the southern half of the sector, which excludes the linear features (green region). We see that there is slightly less power in the southern half of the sector, though given the errors its power spectrum is consistent with that of the whole sector. This

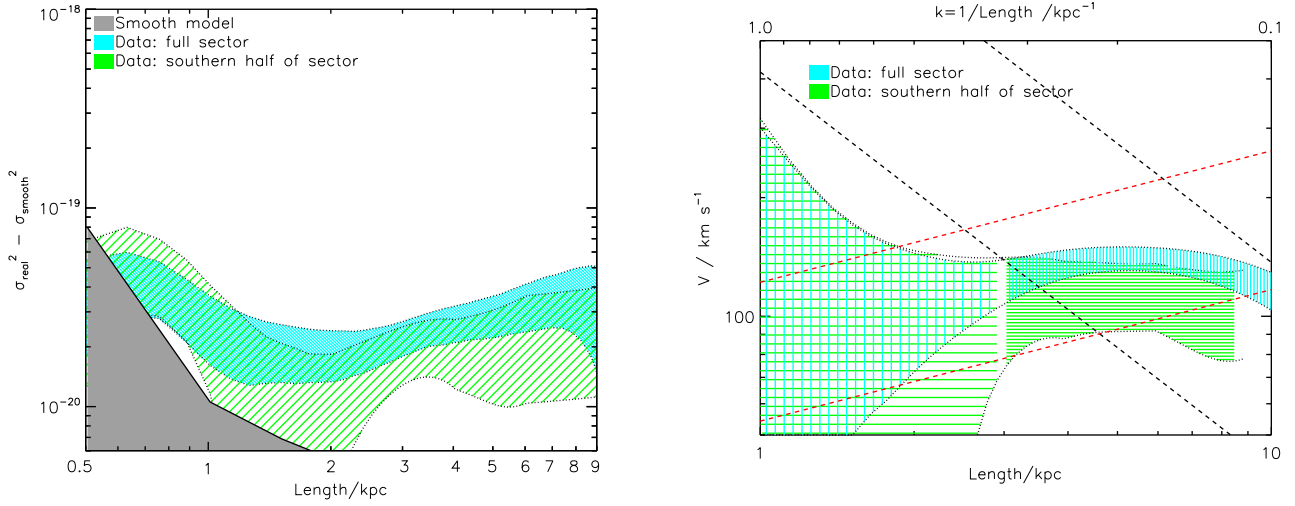


Figure A1. *Left:* Comparing the power spectrum of the surface brightness fluctuations in the southern half of the sector away from any linear features (green line shaded region) with the power spectrum of the whole sector (cyan region). *Right:* Comparing the constraints on the one component velocity of the gas motions as a function of their length scale for the two regions. The black and red dashed lines show the constraints shown earlier in Fig. 6 obtained by considering metal diffusion and the heating-cooling balance.

reduction in power lowers the velocities of the gas motions calculated from the surface brightness fluctuations, as shown in the right hand panel comparing the velocity constraints for the southern half of the sector with the whole sector. Given the errors the two are still consistent with one another, and also still consistent with the constraints on the velocity and length scales obtained by considering metal diffusion and the balance between heating and cooling (dashed black and red lines respectively).